SIMULATION STUDIES FOR SURFACES AND MATERIALS STRENGTH

Semiannual Progress Report

for
Cooperative Agreement NCC2-297

for the period
May 1, 1992 - October 31, 1992

Submitted to

National Aeronautics and Space Administration
Ames Research Center
Moffett Field, CA 94035

Computational Chemistry Branch
Dr. Steve Langhoff, Chief

Thermosciences Division
Dr. Jim Arnold, Chief

Prepared by
Eloret Institute
1178 Maraschino Drive
Sunnyvale, CA 94087
Phone: 408 730-8422 and 415 493-4710
K. Heinemann, President and Grant Administrator
Timur Halicioglu, Principal Investigator

During this period investigations were carried out in three areas:

1. Binding energies and high energy binding sites were calculated for carbon atoms deposited on a (2×1) dimerized Si(100) surface. The location of the energetically most favorable binding site was found to be near the top position of a second layer Si atom with a binding energy of −3.36 eV. Also calculated were excess energies for the substitution of C (replacing Si atoms) in the exposed surface region. For the substitution of a carbon atom in surface layers 1 through 4 calculations produced progressively increasing excess energies from the exposed surface to the interior. This indicates that the diffusion of a substituting C atom from the top layer to the interior via a site exchange mechanism is energetically unfavorable. Computational details along with a short discussion of the results are presented in Appendix I.

2. Structure- and energy-related properties of defects formed on relaxed diamond surfaces were investigated. Simulation calculations were carried out for vacancies created on (111) and on (2×1) dimerized (100) index planes of diamond. Two different model functions (based on two- and three-body interactions) developed recently for carbon were employed in the calculations. Both functions produced comparable results. Top layer vacancies are more likely to form on the (100) surface than on the (111) surface. Calculations indicate that the diffusion of a single vacancy from the top surface layer to the second layer is not energetically favored. For details see Appendix II.

3. In this part, recently developed Tersoff-type model functions for Si were employed to investigate the energetics of the following processes: (1) neutral monovacancy and divacancy formation and migration energies; (2) neutral bond-centered, site sharing, tetrahedral, and hexagonal self-interstitial formation and migration energies; and (3) the variation of these energies with distance from a bulk site of Frenkel defect formation and from [100] and [111] surfaces. All the calculations were performed employing an energy minimization procedure for the low temperature limit. In addition to the energy values, structural changes around defective regions were also calculated for different vacancies and interstitials. Details of this investigation are presented in Appendix III.

APPENDIX I:

Carbon Atoms Deposited on the (2×1) Reconstructed Si(100) Surface

Introduction

An atomic level understanding of the structure of a surface defect and its energetics is highly desired by many surface scientists today [1]. In diamond film synthesis, in particular, it has been shown that defects in the surface region of a substrate play an important role in early stages of the nucleation and growth process [2,3]. Binding energies for carbon atoms on Si substrate surfaces along with the binding sites geometries are very important features which often determine the quality and characteristics of the film.

In this investigation simulation calculations were carried out to analyze energy- and structure-related properties for carbon atoms deposited on a (2×1) dimerized Si(100) surface. In addition to binding energies, substitutional energies were also calculated for C atoms replacing Si atoms in the surface region. All the calculations in this study were carried out for the low temperature limit using a static minimization procedure. Interatomic energies as functions of atomic positions were estimated employing a potential energy function developed recently by Tersoff [4]. This function has been designed specifically for SiC and it has been used successfully in calculating energies and structures for carbon defects in bulk Si [5]. At the same time, it has been shown that for pure Si systems also, the Tersoff function produces acceptable results for various bulk and surface properties [6]. Furthermore, for pure carbon systems this function is able to reproduce correctly many bulk properties of diamond and of the graphitic plane, and recently it has been used to estimate surface properties for low index planes of diamond [7].

Calculations

The Si(100) surface was generated, first, as an abrupt termination of bulk silicon in the diamond cubic structure with a lattice constant corresponding to the equilibrium volume of Si calculated by the Tersoff function. Then, the system was equilibrated producing (2×1) dimerized reconstruction patterns at the exposed (100) surface. In the equilibration process, every atom in the system was permitted to relax by minimizing the total energy with respect to the atomic coordinates. Simulation calculations were carried out considering a computational cell which was made of a slab of 16 atomic layers each containing 16 Si atoms. This cell size was found to be adequate for the present investigation. Calculations for selected cases using larger cell sizes produced virtually identical results. Throughout this study, calculations were performed considering periodic boundary conditions imposed on the system in two directions (parallel to the exposed surface) in order to provide continuity.

The binding energy, ϕ_b, per carbon adatom was calculated as:

$$\phi_b = \frac{1}{m}[E_a^{(m)} - E^o]$$

where m is the number of adatoms, E^o denotes the total equilibrated energy of the system of N particles with clean exposed surfaces, and $E_a^{(m)}$ is the total relaxed energy of the same system with m adatoms deposited on the surface. In calculating binding energies, carbon atoms were first positioned on a fully relaxed surface and then the system was reequilibrated to obtain $E_a^{(m)}$. In order to find adsorption sites with lowest binding energies, calculations were repeated with different initial positions for carbon atom. On a single surface cell 25 different initial configurations were employed and those producing lowest energies were reported here.

In addition to binding energies, we also calculated energies of substitution for C replacing Si atoms in the surface region. Substitutions were made in different surface layers and the system was fully reequilbrated after the substitution. In a manner analogous to the binding energy, the substitutional energy also was considered simply as an excess energy in this investigation and it was calculated as:

$$\phi_x = \frac{1}{n}[E_s^{(n)} - E^o]$$

where ϕ_x represents substitutional excess energy, n is the number of substituting C atoms, E^o denotes the total equilibrated energy of the Si system bearing the exposed surface (as defined above) and $E_s^{(n)}$ is the total relaxed energy of the same system with n substitutional C atoms. In the process of substitution the number of atoms in the system remains unchanged. Furthermore, according to the present definition ϕ_x represents an excess energy, therefore, it does not include formation energies for pure C and Si systems.

Results and Discusion

For a single carbon atom the most favorable binding site on a defect-free (2×1) dimerized Si(100) surface was found to be 'almost' on top of a second layer Si atom between two dimer rows. Schematic top and side views are shown in Figure 1. Due to strong Si−C interactions Si atoms located in the vicinty of C were displaced from their original sites. Upon relaxation all neighboring Si atoms had migrated toward the C atom. In this case, there are three neighboring Si atoms in close proximity to the deposited C atom. The nearest one is located in the second layer at a distance of 1.72 Å. The other two neighbors are in the top surface layer and belong to two different Si dimers. They are equidistant from the C

adatom and the Si–C bonds were calculated as 1.82 Å forming an apex angle of 133 degrees. The binding energy for the carbon atom at this site was calculated as −6.193 eV.

The other energetically favorable binding site for a single C atom is located above the mid-point of a Si dimer. This binding site is 'exactly' above a fourth layer Si atom and it is depicted in Figure 2. In this case, the C adatom has two close neighbors with equal Si–C separations of 1.80 Å. These bonds form an apex angle of 124.5 degrees at the carbon atom position. Under the force field of the carbon atom, the neighboring Si atoms forming the dimer were displaced toward their original (1×1) positions. Here, in its fully relaxed configuration the Si–Si separation was calculated as 3.18 Å, while for the defect-free (2×1) reconstructed Si(100) surface, the Si–Si distance in a dimer is 2.37 Å. The binding energy for a C atom at this site is somewhat higher than the previous case and it was estimated as −5.925 eV.

For two adatoms the energetically most favorable sites are shown in Figure 3. These sites are symmetrically situated along the dimer row and they are basically identical with the high energy position indicated above for the single C atom. The four Si–C distances between the C adatoms and their proximate top layer neighbors in the adjacent Si dimers were calculated as 1.79 Å. Distances between the carbon atoms and their nearest neighbors in the second layers were found to be equal to 1.70 Å. These distances are sligthly shorter than the single carbon atom case mentioned above. The total binding energy per C adatom is −6.30 eV which is somewhat lower than the energy value obtained for a single C atom calculated above. Because of the local symmetry in this case, an additional strain energy was released upon relaxation. The distance between two carbon adatoms is 3.70 Å and obviously at this separation no

contribution is expected coming from the C—C interactions to the total energy.

Next, excess energies for substitution were calculated for a C atom replacing Si within the exposed surface region. Calculations were performed for the (2×1) dimerized (100) surface. Excess energies were estimated for C atom substitutions in the surface layers 1 through 4. Calculated energy values along with some structural parameters are presented in Table 1.

An equilibrated top and side views are depicted schematically in Figure 4 for a single C atom replacing a top layer Si atom. In this case, one of the Si atoms in a dimer is replaced by the carbon atom. In the fully equilibrated configuration the site for the substitutional C atom is about 0.45 Å lower than the top surface layer and the Si—C bond is positioned asymmetrically. See Figure 4. In this dimerized top layer, the substitutional C atom has three neighbors with approximately equal Si—C bond lengths. While one of the Si atoms is in the first layer, the other two are positioned in the second layer. In this case, due to the relaxation in the interlayer spacings, the avarage Si—C—Si angles were found to be around 119 degrees, somewhat larger than the ideal tetrahedral angle.

Each C atom substituting for a Si atom in layers 2 through 4, has four immediate neighbors located in the contiguous layers. Two of them are in the next upper layer and the other two are located in the layer below. For a C atom substitution in the second layer the excess energy was found to be somewhat higher than in the previous case. The average Si—C distances to immediate neighbors are slightly larger. (See Table 1). The Si—C—Si angles which can be regarded as a measure of the tetrahedral symmetry in this case vary within 104 - 113 degrees averaging to a

value of 109 degrees.

On a clean (2×1) dimerized (100) surface all the atomic sites in the top layer are identical. Similarly, in the second layer also all the sites are identical and therefore, they would produce the same excess energy upon a C atom substitution. For the third and fourth layers, however, two different substitutional sites are possible. Figure 5 depicts a schematic top view of a fully relaxed Si(100) surface. Atomic sites up to fourth layer from the top are shown in this figure. The two different substitutional sites for carbon in the third and fourth layers were indicated in Figure 5 by letters a, b and c, d, respectively. Substitutions in sites a and c which are located under the dimer row, produced lower excess energies than the substitutions in sites b and d. The substitution in site a produced a value comparable with the second layer substitutional excess energy obtained above. The value for site b, however, is about 0.85 eV higher. These excess energies give an average ϕ_x value of -2.04 eV for the third layer substitution. A similar trend was obtained for the fourth layer as well. The site c, which is located beneath the mid point of a Si dimer, produced a ϕ_x value which is about 0.76 eV lower then the site d. In this case, an average value of -1.87 eV was obtained for the substitution of C in layer 4. Average Si—C bond lengths for both the third and fourth layers, however, show only small variations. Similarly, changes in the Si—C—Si angles were also found to be very small and calculations for the third and fourth layer cases produced average tetrahedral angles around 109 degrees.

Conclusions

Calculations carried out in this investigation indicate that the deposition of C atoms on a (2×1) dimerized Si(100) surface is energet-

ically quite favorable. For a single C adatom the lowest energy binding site is located near the top position of a second layer Si atom between two Si dimer rows. In this case the local symmetry at the binding site was somewhat distorted and the adjacent Si dimers were tilted toward the C atom. Substitutions of carbon atoms in the top surface layers were also found to be energetically favorable. Due to the strong Si—C interactions after the substitution the local symmetry of the lattice is distorted and in all cases, the neighboring Si atoms were found to be displaced toward the substituting C atom.

Replacements of a Si atom by C in surface layers 1 through 4 produced progessively increasing average excess energies from the exposed surface toward interior layers. Accordingly, the diffusion of a substituting C atom from the top layer to the interior via a site exchange mechanism is energetically unfavorable. Results obtained in this investigation, however, are based strictly on energetics and no entropic aspects were taken into consideration. Therefore, it is recommended that extreme care be exercised when comparing these results with experimental findings.

References

[1] V. Bortolani, N. H. March and M. P. Tosi (eds), *Interaction of Atoms and Molecules with Solid Surfaces*, Plenum Press, New York, 1990.

[2] J. W. Kim, Y. J. Baik and K. Y. Eun, Diamond and Related Materials, 1, 200 (1992).

[3] P. Ascarelli, S. Fontana, G. Cossu, E. Cappelli and N. Nistico, Diamond and Related Materials, 1, 211 (1992).

[4] J. Tersoff, Phys. Rev., B 39, 5566 (1989).

[5] J. Tersoff, Phys. Rev. Lett., 64, 1757 (1990).

[6] H. Balamane, T. Halicioglu and W. A. Tiller, Phys. Rev., B, 46, 2250 (1992).

[7] T. Halicioglu, Surf. Sci., 259, L714 (1991).

Table 1. Calculated values for the replacements of Si atoms by C in the top four layers of the Si(100) surface. The excess energy for C substitution, the average Si−C distance and the number of near neighbors are denoted by ϕ_x, d_{Si-C} and N_i, respectively. For the third and fourth layers different substitutional sites indicated by letters a through d are shown schematically in Figure 5. (For first and second layers all sites are identical).

Layer Number	Site	ϕ_x (eV)	d_{Si-C} (Å)	N_i
1	0	−3.36	1.85	3
2	0	−2.45	1.91	4
3	(a)	−2.47	1.93	4
3	(b)	−1.61	1.95	4
4	(c)	−2.25	1.94	4
4	(d)	−1.49	1.97	4

Figure Captions

Figure 1. Schematic (a) top and (b) side views showing the energetically most favorable site for a carbon adatom deposited on a (2×1) reconstructed surface of Si(100). Si atoms in dimers are connected with solid lines and dotted lines indicate bonds between the top layer atoms and atoms located in the second layer. Large, medium and small open circles indicate sites for Si atoms located in the first, second and third layers, respectively. The deposited carbon atom is represented by a large shaded circle.

Figure 2. Schematic (a) top and (b) side views for a carbon atom deposited on the Si(100)-(2×1) surface. The carbon adatom, in this case, is located above the mid-point of a Si dimer. (Symbols are explained in the caption for Figure 1.)

Figure 3. Two carbon atoms deposited on a Si(100)-(2×1) surface. Top and side views are depicted in a and b, respectively. (Symbols are explained in the caption for Figure 1.)

Figure 4. In the top layer of a Si(100)-(2×1) surface a single C atom is shown substituting for a Si atom. Top and side views are depicted in a and b, respectively. (For symbols see the caption of Figure 1).

Figure 5. A schematic top view for a fully relaxed (2×1) dimerized Si(100) surface. Large, medium and small open circles indicate Si atoms located in the first, second and third layers, respectively. Small solid circles represent Si atoms in the fourth layer. Letters a, b and c, d indicate different sites for Si atoms located in the third and fourth layers, respectively.

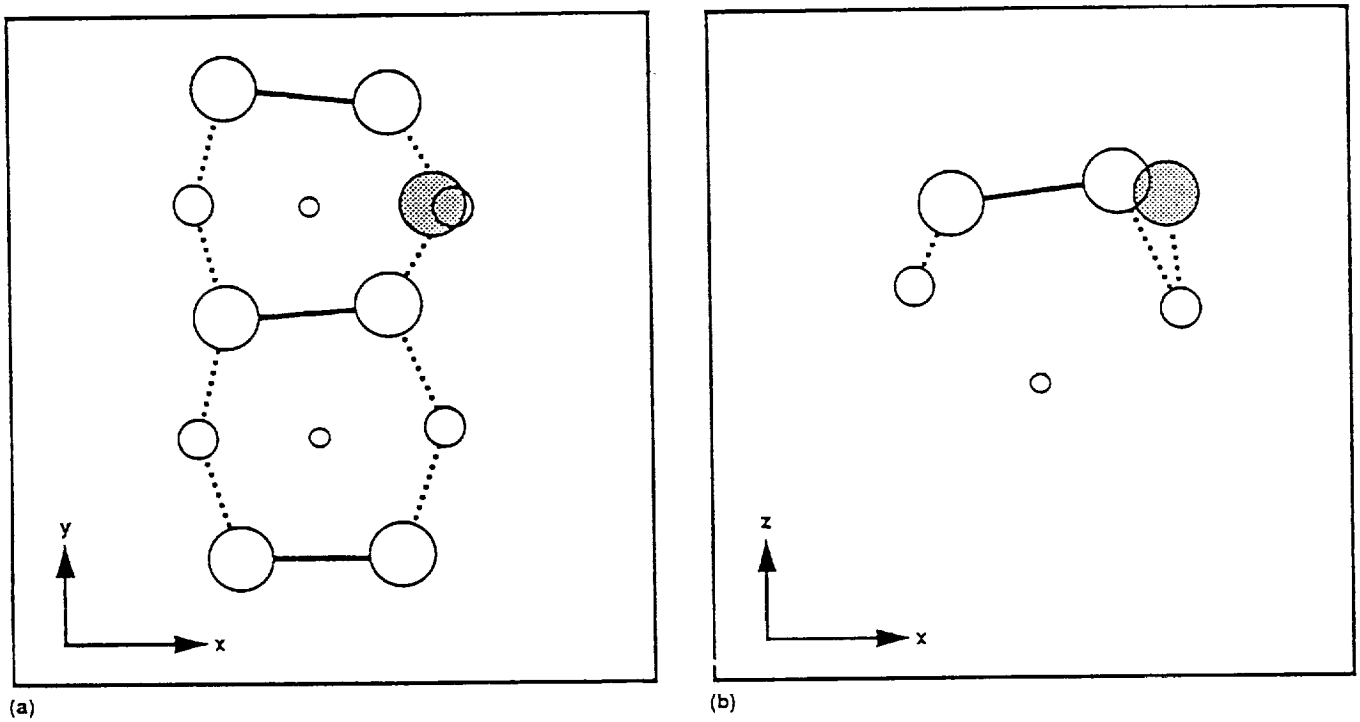

Figure 1

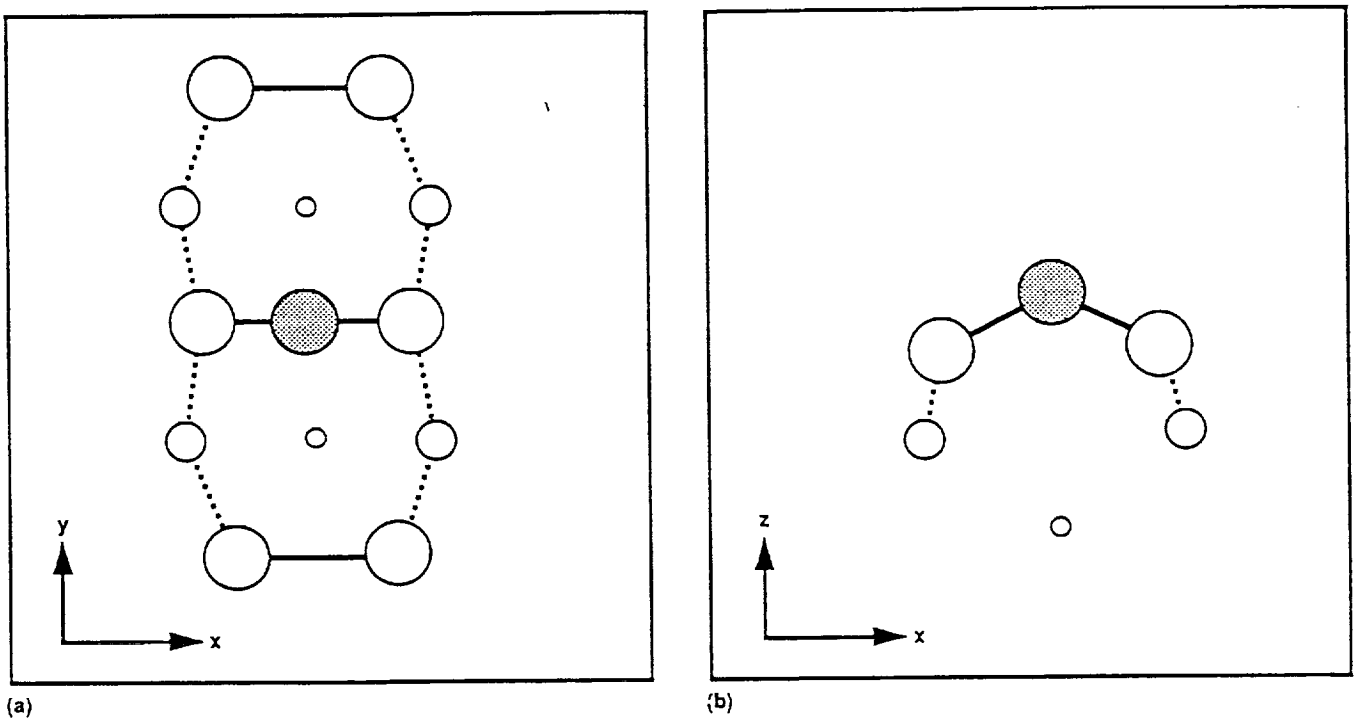

Figure 2

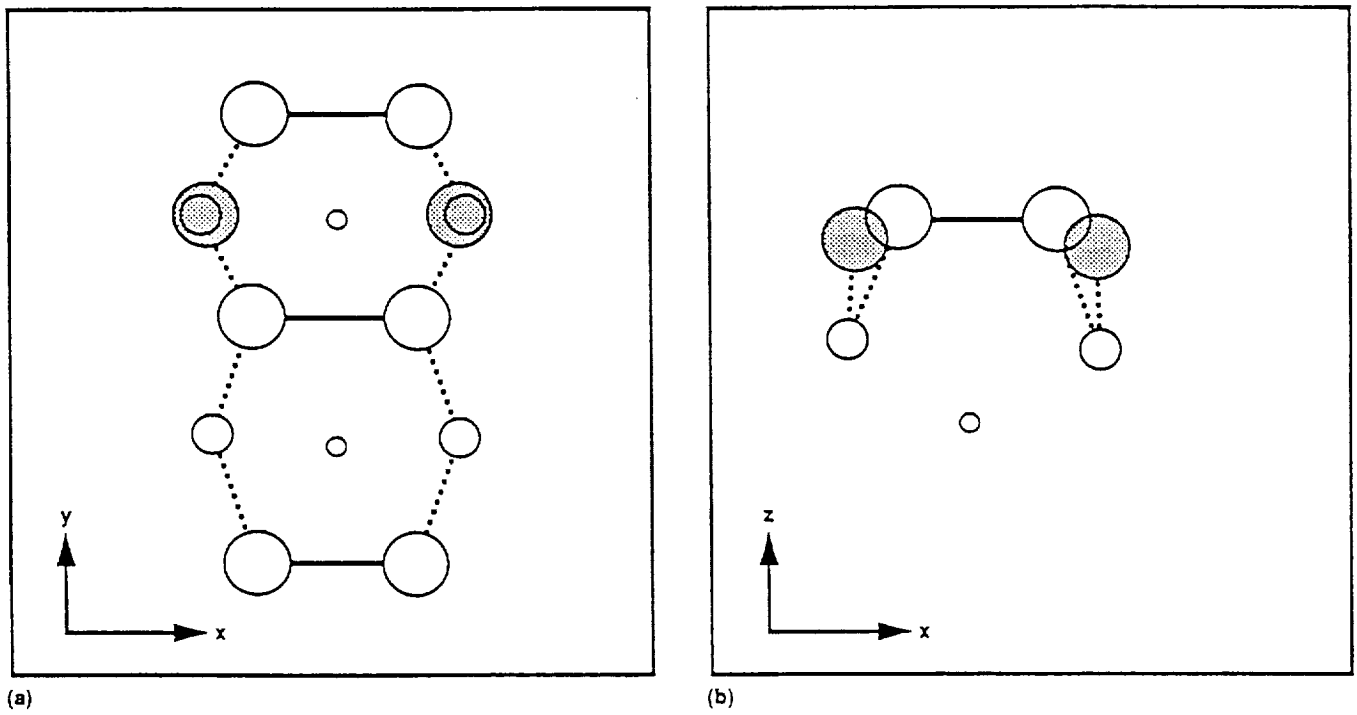

Figure 3

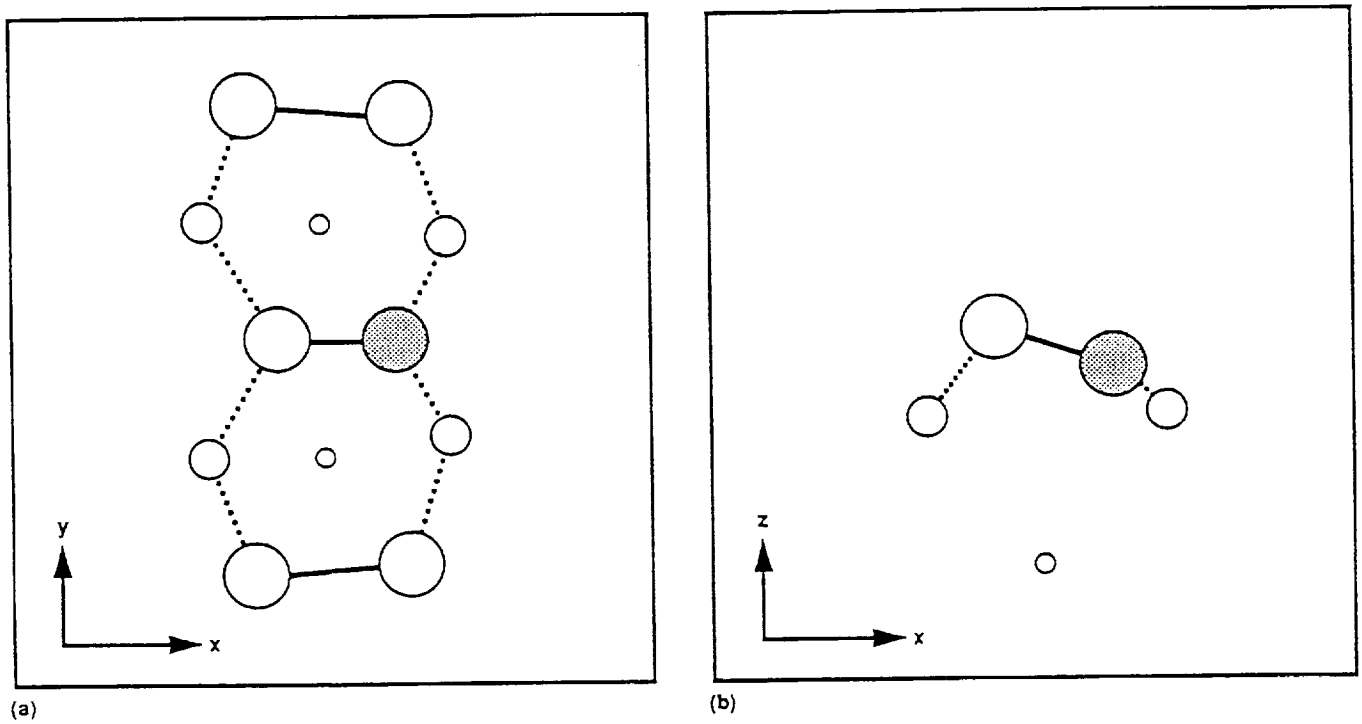

Figure 4

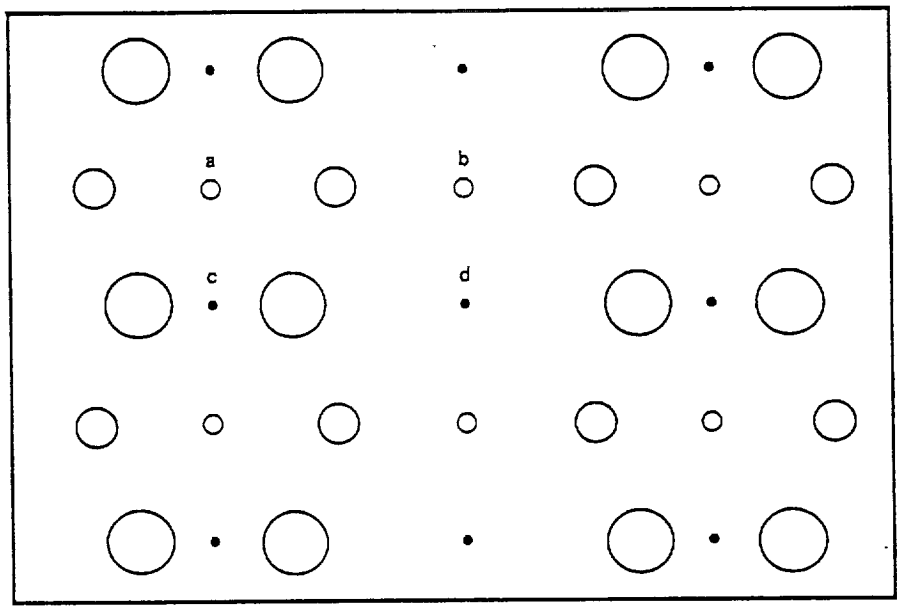

Figure 5

APPENDIX II:

Calculations for Defects Formed on Diamond Surfaces

Introduction

Surface defects play a significant role in research areas related to nucleation and growth phenomena. An understanding of defects at microscopic dimensions is highly desired by surface scientists today. In general, it is believed that the local structure of a surface defect is an important factor controlling nucleation and the early stages of the growth process [1,2]. Presently, there is not enough information available on the energetics and the local structure of defects formed on diamond surfaces. Computer simulation techniques based on atomic considerations provide a very useful approach to the study of various processes taking place on surfaces.

In this work, a simulation study is conducted to investigate structure- and energy-related properties of defects formed on the relaxed (111) surface and on the (2×1) dimerized (100) surface of diamond. Simulation calculations were performed for the low temperature limit (i.e., T=0 K) using a static minimization procedure. To calculate configurational energies model potential functions developed recently for carbon species were used throughout this study. For a better analysis, two different model functions, based on two and three-body interactions, were considered here. The first potential is the Tersoff function [3]. It has been shown by Tersoff that this function is able to reproduce correctly various bulk properties of diamond and of the graphitic plane. The second potential used in this study is the Brenner function [4] which is analytically similar to the Tersoff function, but parametrized differently. This function also, has been shown to produce acceptable results for properties of bulk diamond and the basal plane of graphite, as well as for some properties of small carbon clusters [4,5]. While the Tersoff function reproduces correctly the lattice constant

of diamond, the Brenner potential at its minimum energy configuration gives a lattice constant value about 3% shorter. However, structural properties for small clusters of carbon are better represented by the Brenner function [5]. These functions have also been used recently to calculate defect-free surface properties for low index planes of diamond [6].

Method of Calculation

In this study structure- and energy-related properties of small vacancies created on the (111) and (100) surfaces of diamond were investigated. Calculations were carried out considering a computational cell containing more than 500 carbon atoms in a diamond cubic structure. The system was positioned in two different ways to provide the desired (111) and (100) index planes with layers parallel to the exposed surface, each containing 32 carbon atoms. Periodic boundary conditions were imposed on the system in two directions (parallel to the exposed surface) in order to provide continuity. These systems then were fully equilibrated to obtain relaxed surfaces. For the (100) surface the equilibration was carried out to produce a (2×1) dimerized reconstruction pattern. Defects were created on these relaxed surfaces and then the system was reequilibrated to obtain relaxed defect energies and geometries.

In all cases, defect energies were calculated as:

$$E_v = \Phi_v - \Phi_o + (N_1 - N_2) \times e_{coh}$$

where, E_v is the surface vacancy formation energy, Φ_o denotes the total relaxed energy of the defect-free system with an exposed surface. Φ_v is the total relaxed energy of the same system with surface vacancies. e_{coh} represents the cohesive energy of bulk diamond calculated by the poten-

tial function. N_1 and N_2 denote respectively the number of carbon atoms in the system before and after the formation of the defect. To analyze the extent of the relaxation taking place during the reequilibration process we also calculated the unrelaxed energy, E_v^U, for defects. In this case, E_v^U is calculated using the unrelaxed value of Φ_v before the reequilibration. Accordingly the relaxation energy for the vacancy is defined as the difference between E_v^U and E_v.

Results

For the (2×1) dimerized (100) surface, vacancy energies calculated using Tersoff and Brenner functions are given in Table 1. A schematic top view of the dimerized (100) surface and various defect structures are shown in Figure 1. For a single vacancy created at the top layer, both the Tersoff and Brenner functions produce relatively low formation energies. The value calculated by the Tersoff function is somewhat lower than the value obtained by the Brenner potential. In both cases, however, the relaxation lowered vacancy energies considerably. For the dimerized (100) surface, upon creating a single vacancy at the top layer, one carbon atom is left unpaired. During the reequilibration process it was found that this unpaired C atom moves to its original (1×1) position, which is right above the mid-point between two second layer C atoms (see Figure 1b).

Both potential functions produced much larger energy values for a single vacancy created in the second layer. In this case, the Brenner function predicts somewhat lower energy than the Tersoff function and relaxation energies associated with the vacancies are quite large. After the reequilibration, C atoms adjacent to a second-layer vacancy were found to be displaced radially outward. The two C atoms closest to the

vacant site are located in the top layer. During the reequilibration process these two carbon atoms migrated outwards (in the direction away from the vacancy center) about 0.25 and 0.32 Å for the Tersoff and Brenner functions, respectively. The top view of this relaxed configuration is shown schematically in Figure 1c.

A dimer vacancy was generated in the top layer by removing both carbon atoms of a dimer. This is shown in Figure 1d. Calculations for a dimer vacancy produced very low energy values. While the Tersoff function produced a dimer vacancy energy comparable to the energy of a single vacancy, the Brenner function predicts even a lower energy value for a dimer vacancy. (See Table 1). In this case the Brenner function predicts that the formation of a dimer vacancy is energetically more probable than the formation of a single vacancy. Accordingly, for a dimer vacancy a considerable amount of relaxation energy is released (in particular for the Brenner potential) during the reequilibration.

Energy values calculated for vacancies formed on the (111) surface of diamond are given in Table 2. Also, schematic top views for relaxed vacancy configurations are depicted in Figure 2. In all cases, vacancy energies for the (111) surface were found to be larger than the energies calculated for the (100) surface vacancies. In general, the Brenner function predicts somewhat smaller vacancy energies than the Tersoff potential. Similar to the previous case, carbon atoms adjacent to the vacant site were found to be displaced outwardly upon relaxation. For a single vacancy created at the top layer, the displacements were calculated as 0.16 and 0.10 Å for the three second layer atoms closest to the vacancy site using the Tersoff and Brenner functions, respectively. This is shown in Figure 2b. For a single vacancy formed in the second layer the outward displacements for the three first layer carbon

atoms are 0.18 and 0.09 Å for the Tersoff and Brenner functions, respectively. (See Figure 2c). For a two-vacancy defect formed by removing two neighboring carbon atoms from the top layer, atoms adjacent to the vacant site were also relaxed outwardly as shown in Figure 2d. The displacements of these atoms upon relaxation are comparable to those of the top layer single vacancy case mentioned above.

Conclusions

Qualitatively speaking both potential functions produced consistent results which indicate that vacancies are more likely to form on the (100) surface than on the (111) surface. Calculations by both functions indicated very low formation energies for dimer vacancies on the (100) surface in particular. Based on energetic considerations, therefore, a higher concentration of vacancies is expected on the (100) surface. In all cases, energies calculated for single vacancies in the second layer were found to be higher than energies for single vacancies in the top layer. In general, energy differences are $\sim$ 2 eV or higher indicating that a single vacancy diffusion from the top layer to the second layer is an energetically unfavorable process. In all cases, atoms adjacent to a defect site were found to relax outwards (i. e., in the direction away from the vacant center). Atoms second neighbors to a vacant site however, exhibited only very minimal displacements during the relaxation.

Present results may serve to build reliable models for the interpretation of experimental observations. Despite the fact that calculations carried out here are for the low temperture limit, they are based on potential functions which are shown to reproduce many properties of diamond correctly.

References

[1] K. Wandelt, Surf. Sci., **251/252** (1991) 387.

[2] V. Bortolani, N. H. March and M. P. Tosi (eds), *Interaction of Atoms and Molecules with Solid Surfaces*, Plenum Press, New York, 1990.

[3] J. Tersoff, Phys. Rev. Lett., **61** (1988) 2879.

[4] D. W. Brenner, Mater. Res. Soc. Symp. Proc., **141** (1989) 59.

[5] T. Halicioglu, Chem. Phys. Lett., **179** (1991) 159.

[6] T. Halicioglu, Surf. Sci., **259** (1991) L714.

Table 1. Calculated formation energies for vacancies on the (2×1) dimerized (100) surface of diamond. E_v^U and E_v denote unrelaxed and relaxed energies in eV.

	Tersoff		Brenner	
	E_v^U	E_v	E_v^U	E_v
Single Vacancy (Top Layer)	2.168	0.432	2.686	0.941
Single Vacancy (Second Layer)	5.062	3.212	4.385	2.917
Pair Vacancy (Top Layer)	1.562	0.483	2.681	0.317

Table 2. Calculated formation energies for vacancies on the (111) surface of diamond. E_v^U and E_v denote unrelaxed and relaxed energies in eV.

	Tersoff		Brenner	
	E_v^U	E_v	E_v^U	E_v
Single Vacancy (Top Layer)	3.930	2.939	2.752	2.022
Single Vacancy (Second Layer)	7.090	5.657	5.892	5.189
Pair Vacancy (Top Layer)	7.924	6.208	5.968	4.498

Figure Captions

Figure 1. Schematic top views for the (2×1) dimerized (100) surface of diamond. (a) defect-free surface, (b) single vacancy in the top layer, (c) single vacancy in the second layer and (d) dimer vacancy in the top layer. Large and small circles represent carbon atoms located in the top and second layers, respectively.

Figure 2. Schematic top views for the (111) surface of diamond. (a) defect-free surface, (b) single vacancy in the top layer, (c) single vacancy in the second layer and (d) double vacancy in the top layer. Large and small circles represent carbon atoms located in the top and second layers, respectively. Arrows indicate atomic motions in lateral directions during relaxation.

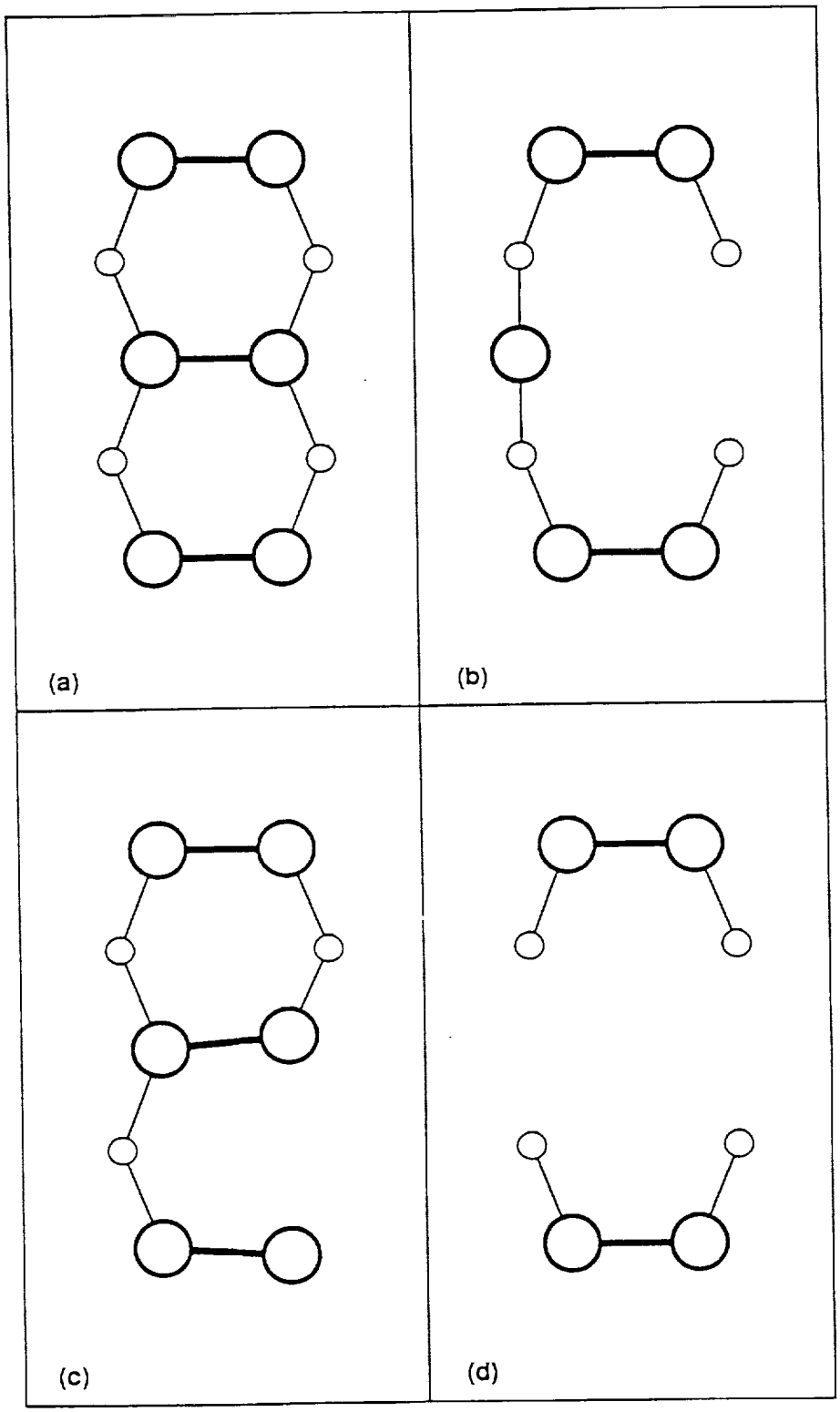

Figure 1.

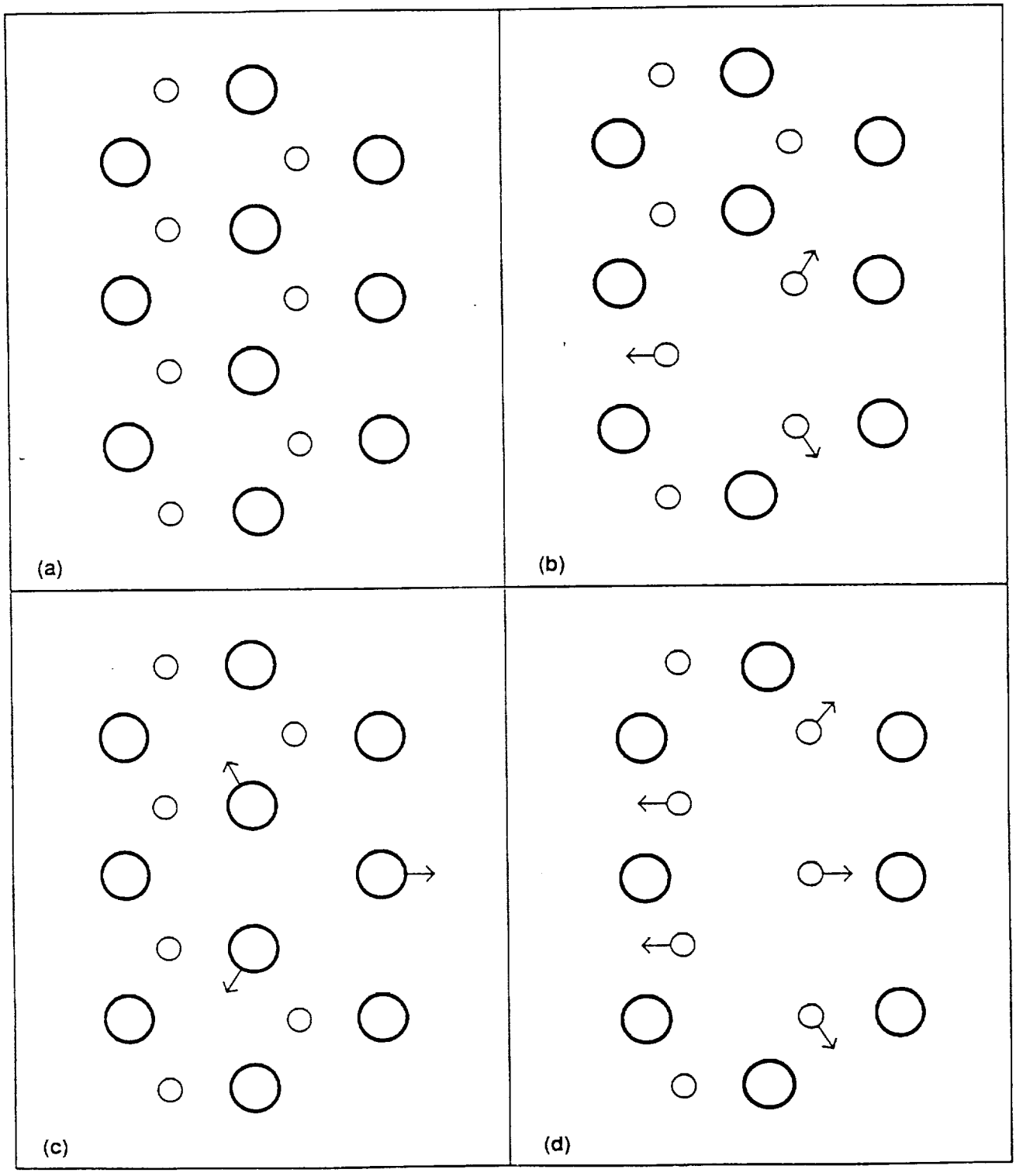

Figure 2.

APPENDIX III:

Point Defect Structures and Energetics in Si Using an Empirical Potential

Introduction

A recent comparative study of six different empirical potential energy functions for silicon [1] showed that each served best for a unique range of application and conditions but no single potential of this set gave excellent fit over the broad range of applicability for which such potentials might be used; i.e., clusters, bulk, surfaces, defects, and so on. This study [1] showed that the Tersoff potentials [2,3] were acceptable choices for the investigation of point defects and elastic properties, although they have very short range and do not provide perfect matches with some ab initio results [1] (such as predicted structures of Si_{3-6}). In spite of their few shortcomings, we find it is useful to employ such potential energy functions (PEFs) for considering atomic structure variations around point defects and for investigating how the energetics of these defects change with respect to distance from a surface or from a site of Frenkel defect formation.

In this paper, we use the Tersoff 2 (T2) and Tersoff 3 (T3) potentials [4] to perform statics calculations (representing the low temperature limit) for the energetics of the following processes: (i) neutral monovacancy and divacancy formation and migration in Si; (ii) neutral bond- centered, site-sharing, tetrahedral, and hexagonal self- interstitial formation and migration; (iii) the variation of these energies with distance from a bulk site of Frenkel defect formation as well as from [100] and [111] surfaces. In a subsequent paper, the temperature dependence for these different defects will be presented where, in Monte Carlo simulations, one can see the structural transition from one kind of defect to another within a specific temperature range. Such interesting temperature-dependent behavior with its associated structural details is not available today from purely ab initio treatments [5-9].

This is one of the definite advantages of the empirical PEF approach compared to present-day ab initio approaches. It is also curious to note that the empirical PEF technique seems to provide activation enthalpies for point defect formation in Si that are closer to experimental values than do the ab initio calculations [10].

Procedure

In the present work, we have effectively confined our calculations to the low temperature limit by employing the Fletcher-Reeves-Polak-Ribiere conjugate gradient technique [11] to perform static energy minimization for configurations of Si atoms as part of two kinds of static simulations. The first is a straightforward formation energy calculation in which a defect is created and the atoms are then relaxed to what should be the minimum energy state. This relaxed energy is then compared to a similar system without the defect. The second is an extension to formation energy calculations wherein we study the process by which a created defect migrates from site to site.

The formation energies per defect, ΔE_f, reported on here for vacancies and self-interstitials are calculated using

$$\Delta E_f = E_d - \frac{N_d}{N_b} E_b \tag{1}$$

where E_d and E_b are the energies of the system with and without the defect, respectively, while N_d and N_b are the total numbers of atoms in each system. For a vacancy, the formula assumes that the absent atom has moved out of the computational cell to a surface kink site where it contributes to the total binding energy without altering the energetics of the surface. For an interstitial, the process is reversed and an atom is removed from a surface kink site to an interior site within the computational cell.

To calculate activation barriers for point defect migration, the program moves an atom along a specified path and, at each point along the path, it uses static minimization to calculate the relaxed energy of the system with the constraint that the advancing atom is (temporarily) held fixed. After each minimization, the other atoms return to their initial positions, and the moving atom advances to the next point on the path. Our intention is to simulate the process by which a defect is created or an existing defect migrates from point to point, and hence to estimate the potential energy barrier for this process to occur.

The selection of the path on which to move the atom can be a study in itself. Ideally, the atom should experience no component of force perpendicular to the path before or after relaxation of the surrounding atoms, since a non-vanishing perpendicular force implies that there is a neighboring path with lower energies connecting the same two endpoints. This condition means that appropriate paths follow the flow lines of the 3-D force field. Not all flow lines are appropriate, however, since the potential should have positive curvature perpendicular to the path so that it is stable. If the curvature is negative along a perpendicular direction, then the selected flow line effectively runs along the crest of a ridge, and is an unlikely candidate. Essentially, we are searching for a sequence of flow lines that connect a pair of stable sites through one or more saddle points that are energy maxima along the path and are stable perpendicular to the path. These saddle points are states at the top of the energy barriers along the path.

The common method of doing activation barrier calculations is that of constrained optimization, which avoids selection of the path in advance by moving the atom along one direction while allowing it to relax in the perpendicular plane. The atom then follows its own path, but not

necessarily one that satisfies the conditions just described. Moreover, the greater the relaxation of the advancing atom in the perpendicular plane, the more the conditions are violated. We feel it is better to spend more effort preselecting an appropriate path. Fortunately, the path required to simulate the migration of, for example, a monovacancy is straight and very short. Furthermore, we have found that a path constructed with linear segments connecting neighboring tetrahedral sites is often satisfactory for longer paths in the bulk due to the short range of the potential and to the remaining symmetry of the crystal, even with a defect. On the other hand, a piece-wise linear path can be unsatisfactory for migration from a surface, for example, where the symmetry is broken. More sophisticated path selection methods are possible, but we have not tried them here.

Results

A. Point Defect Energies and Structures

The formation energies, E_f , and relaxation displacements, δ_i, of adjacent atoms for several point defects are given in Table I. Figures 1 and 2 provide representations of some different local atomic configurations encountered. The tetrahedral (T) and split (S) monovacancy structures plus the stable (D) and metastable (D') divacancy structures are given in Figure 1. During relaxation, the atoms neighboring the T-vacancy move outwards while they move inwards for the S-vacancy. We attribute this difference to the presence of a central atom in the split form that pulls surrounding atoms inward to help fill the void. We see from Table I that the S-monovacancy has the smaller total energy at the expense of increased atomic displacement. For the different interstitial species, Figure 2 illus-

trates the different types of displacements, δ_i, listed in Table I.

B. Point Defect Migration

Figure 3a illustrates the path used to simulate the migration of a monovacancy. Figures 4a and 4b represent the simulation results for the T2 and T3 PEFs, respectively. From 0 to 1 on the abscissa corresponds to a displacement of 2.35 Å (from one tetrahedral site to another). Note that the vacancy structure switches discontinuously from the tetrahedral structure to a split form near mid step. For the T-vacancy, the moving atom initially has three neighbors, while for the S-vacancy it has six. It is precisely when the moving atom encounters the additional neighbors that a jump in energy and a change in structure occurs.

In this case, such behavior is a probable consequence of the short range and sharp cutoff function characteristics of the Tersoff potentials, as well as the limitations of the static minimization procedure. For example, if the relaxation of a configuration of atoms to its lowest energy state requires more than a small motion of any of the atoms, then the conjugate gradient procedure (as well as any other multidimensional static minimization technique) is likely to relax the atoms into a metastable state, since it cannot "see" the lower energy state. Other problems arise from the form of the cutoff function in the transition region of width μ from $R_c - \mu$ to R_c. Although the function is smooth, its transition to zero is very sharp and its slope has corners at the endpoints of this region (i.e., the second derivative is discontinuous), which can be problematic for routines using the gradient directly or indirectly by quadratic interpolation. The cutoff function may be modified to eliminate this behavior, but we have not done this for the work presented here. We have instead monitored the number of neighbors of a

defect atom (for example, the moving atom in a migration calculation) both before and after relaxation of the lattice. If the number of neighbors changes, either during relaxation or as a migrating atom moves, then there is the possibility that the energy and structure will exhibit large changes due to the nature of the cutoff and the limitations of the simulation method.

In spite of the difficulty in providing an unambiguous interpretation, the migration barriers are found to be 0.25 eV and 1.60 eV for T- and S-vacancies, respectively, with the T2 PEF, and 2.5 eV and 2.7 eV for T- and S- vacancies, respectively, with the T3 PEF. (These values were obtained from the energy versus position data generated by the program.) The energies along the migration path are higher for the T3 potential than for the T2 potential because T2 underestimates bond-bending forces (the shear modulus computed for a single crystal with the T2 potential is an order of magnitude lower than the accepted value), while T3 gives a much better match [2,3,12,13].

Figure 3b shows the process used to model the divacancy migration. An atom adjacent to one of the vacant T-sites moves straight to the nearest open site, which forms a metastable divacancy, and then continues to the next vacant site for a net shift of the divacancy center. This described path may not be a true flow line with vanishing perpendicular force; however, only small changes in energy were observed when attempting to refine the path by using constrained optimization. The migration energies for divacancies are shown in Figures 5a and 5b for the T2 PEF and the T3 PEF, respectively. Note that the migration is a two-step process and that each step is similar to the migration of a monovacancy. The activation barriers for divacancy migration were found to be 2.2 eV for the T2 PEF and 3.6 eV for the T3 PEF using T-vacancies.

The migration of a self-interstitial atom from one tetrahedral site to another was simulated yielding the results given in Figure 6a for the T2 PEF and Figure 6b for the T3 PEF, respectively. The calculation includes all three of the bond-line interstitial types since the nominal H*- and H-sites are on the line connecting adjacent tetrahedral sites. Although milder, the discontinuities in the relaxed energy are due to the reasons already discussed for the vacancy defect. Generally, we cannot unambiguously favor one portion of the curve over another, but in the case of a discontinuity as narrow as the pedestal in Figure 6a (less than 0.02 Å) not only would a classical simulation at temperatures greater than zero wash it out completely, but also the atom will not be confined to such a small region quantum mechanically since the corresponding uncertainty in the momentum of the atom will be large. If we eliminate the sharp pedestal, the revised estimate of the T-interstitial formation energy is 4.0 eV for T2, although this structure is no longer expected to be stable. The migration barriers are 0.5 eV for the H*-interstitial for T2, and 1.1 eV for the T-interstitial for T3. Other barriers are listed in Table II.

Figure 7 shows how the program simulates the migration for the S-interstitial. The atom labeled "1" moves into the vacant T-site (shown as a thin, white circle), which causes the other atom in the split interstitial (labeled "2") to move to a nearby T- or H*-interstitial position. The S- interstitial is thus converted to one of the other interstitials. This is one half of the process; the other half of the process is the analogous inverse process that converts the simple interstitial into an S-interstitial at an adjacent location. The activation barriers for the total process are given in Table II.

The energy profiles for point defect movement inwards from the sur-

face for the two PEFs and the two selected surface orientations are given in Figure 8 for T-vacancies and Figure 9 for T-interstitials. We see that these profiles are fully stabilized at roughly 3 atomic distances from the surface. There is evidence of low energy states in the surface layers where defects would, therefore, tend to concentrate. The [100], T2 calculations actually exhibit negative vacancy and interstitial formation energies (clipped on the graphs) near the surface layer, which implies that the surface is ripe for reconstruction using these parameters. Finally, the energy profile for the T- vacancy and T-interstitial formation as a function of distance from a Frenkel defect formation site is presented in Figure 10. The activation energy for formation of this type of defect is 1.0 eV for T3 but only 0.38 eV for T2.

The intricate detail in the curves in Figures 8-10 is the result of the short range of the PEFs. As an atom moves along the bond line from a tetrahedral site, it first comes under direct influence of the atoms in the hexagonal ring surrounding the H-site, then it flips through the ring (i.e., it moves across the H-site), and continues to the next T-site. Since the potentials that we used have short ranges, the number of neighboring atoms (as well as which atoms are the neighboring atoms) that contribute to the energy changes significantly; a potential with greater range would wash out some of this detail by averaging into the calculation significant contributions from neighbors beyond the first shell.

In the development of both PEFs, cohesive energy data for real and hypothetical bulk structures, the bulk modulus, and the bond length in the diamond structure were used [2,3]. However, the T3 results are preferable to the T2 results, because the T3 PEF satisfies the added constraint that it reproduce all three elastic constants of bulk sili-

con to within 20%. This greatly improves the shear modulus, which is too low by an order of magnitude using T2.

For an example calculation with the T3 results, Table I shows that the S-vacancy and the T-interstitial have the lowest formation energies for $T \rightarrow 0$K. Assuming that the formation entropy for all point defects is $\Delta S_f \approx 5k_B$, we have

$$C^*(T) = N_s exp(\Delta S_f/k_B) exp(-\Delta H_f/k_B T) \tag{2a}$$

$$C^*_{V^\circ}(T) = 7.5\times10^{24} exp(-3.52eV/k_B T) cm^{-3} \Rightarrow C^*_{V^\circ}(T_M) = 2.78\times10^{14} cm^{-3} \tag{2b}$$

$$C^*_{I^\circ}(T) = 7.5\times10^{24} exp(-3.48eV/k_B T) cm^{-3} \Rightarrow C^*_{I^\circ}(T_M) = 3.75\times10^{14} cm^{-3} \tag{2c}$$

for the equilibrium vacancy and interstitial concentrations, respectively, as functions of temperature and at the melting point, $T_M = 1683$, and where $N_s = 5\times10^{22}\ cm^{-3}$.

The actual picture is a little different from this because charged vacancy species must also be taken into account. The energy levels in the silicon band gap for these species are known [14] and it can be shown that at the Si melting temperature, the total vacancy content, $C^*_{V(tot)}$), is given by [15]

$$C^*_{V(tot)}(T_M) = C^*_{V^\circ} + C^*_{V^-} + C^*_{V^=} + C^*_{V^+} \approx 20 C^*_{V^\circ}(T_M) \tag{3}$$

If there are analogous levels in the band gap for the charged interstitial states, these are not known at the present, so we shall assume

that equations 2b represent the total interstitial content at T_M. In such a case, Frenkel defect annihilation for $T < T_M$ will occur between $\sim 5 \times 10^{15}\ cm^{-3}$ total vacancies and $\sim 3.75 \times 10^{14}\ cm^{-3}$ neutral interstitials grown-in at $T = T_M$ leaving a net vacancy excess of $\sim 4.6 \times 10^{15}\ cm^{-3}$ vacancies at lower temperatures. Of course, calculations of the thermochemical properties as a function of temperature will yield slightly different results, but these numbers might be considered to be "ball park" estimates.

With respect to defect migration using T3, the T-vacancy is the most stable monovacancy with a migration energy of 2.5 eV, while the S-interstitial variety is a faster moving species with an activation energy of 0.27 eV, although its equilibrium population will be appreciably lower than the T-interstitial species. We must await higher temperature calculations to determine which of these defect types maintain entropically distinguishable features, and thus which are stable defects that are present in the lattice and actively involved in transport.

IV. Conclusions

It is important to recognize that these 0 K energy barriers, as calculated by the present procedures, cannot be expected to correspond always to what high temperature simulations calculate as the activation energy for the process. It is this latter quantity that will be accessible experimentally. The prime value of the present work thus lies in its internal comparison between different defects rather than its match with experimental data.

Preferring the T3 PEF for point defect calculations to the T2 PEF, the S- and T-monovacancies are found to have comparable $\Delta E_f + \Delta E_m$ values with $\Delta E^T_{f,V} = 3.70$ eV, $\Delta E^S_{f,V} = 3.52$ eV, $\Delta E^T_{m,V} = 2.50$ eV, and

$\Delta E^S_{m,V} = 2.70$ eV . The main distinguishing feature between these two species is that the first neighbor shell of atoms relaxes outwards for the T-vacancy and inwards for the S-vacancy. A somewhat similar situation exists for the T-, H*-, and S- interstitials with $\Delta E^T_{f,I} = 3.48$ eV, $\Delta E^{H*}_{f,I} = 4.08$ eV, $\Delta E^S_{f,I} = 4.41$ eV, $\Delta E^T_{m,I} = 1.1$ eV, $\Delta E^{H*}_{m,I} = 0.56$ eV and $\Delta E^S_{m,I} = 0.27$ eV. We find the H-interstitial to be unstable ($\Delta E^H_{m,I} \approx 0$ eV) and the first neighbor shell of atoms relaxes outwards for all species. It was also found that the activation energy for T-T Frenkel defect formation is 1.0 eV and that the variation of the above energies occurs only within ~2-3 atomic distances of a [111] or [100] surface.

References

[1] H. Balamane, T. Halicioglu, and W. A. Tiller, Phys. Rev., B **46**, 2250 (1992).

[2] J. Tersoff, Phys. Rev., B **37**, 6991 (1988).

[3] J. Tersoff, Phys. Rev., B **38**, 9902 (1988).

[4] T-II and T-III were originally designated as Si(B) and Si(C), respectively, in references 2 and 3.

[5] R. Car, P.J. Kelly, A. Oshiyama, and S.T. Pantelides, Phys. Rev. Lett., **54**, 360 (1985).

[6] G.A. Baraff, and M. Schluter, Phys. Rev., B **30**, 3460 (1984).

[7] Y. Bar-Yam, and J.D. Joannopoulos, Phys. Rev., B **30**, 1844 (1984).

[8] P.J. Kelly, R. Car, and S.J. Pantelides, in Defects in Semiconductors, Materials Science Forum 10-12, edited by H.J. von Bardeleben (Trans Tech, Aedermannsdorf, Switzerland, 1986), p. 115 and references therein.

[9] P.J. Kelly, and R. Car, Phys. Rev., B **45**, 6543 (1992).

[10] P.M. Fahey, P.B. Griffin, and J.D. Plummer, Rev. Mod. Phys., **61**, 289 (1989).

[11] W.H. Press, B.P. Flannery, S.A. Teukolsky, and W.T. Vetterling, Numerical Recipes in C, (Cambridge University Press, New York, 1988), p. 317.

[12] G. Simmons and H. Wang, Single Crystal Elastic Constants and Calculated Aggregate Properties: A Handbook, (MIT Press, Cambridge,

1971).

[13] O.N. Neilsen and R.M. Martin, Phys. Rev., B **32**, 3792 (1985).

[14] J.A. Van Vechten, Handbook on Semiconductors: Vol. 3, Materials Properties and Preparation, vol. ed., S.P. Keller; Series ed., T.S. Moss (North Holland, New York, 1980) p. 82.

[15] W.A. Tiller, The Science of Crystallization: Microscopic Interfacial Phenomena, (Cambridge University Press, Cambridge, 1991) p. 275.

[16] See, for example, H.F. Davis and A.D. Snider, Introduction to Vector Analysis, 4th ed., (Allyn and Bacon, Boston, 1979).

[17] Reference 11, pp. 609-632.

Table Captions

Table I: This table shows the defect formation energies, ΔE_f, defined by equation 1, and the relaxation displacements of the atoms near the defect, δ_i, (in order i=1,2,... corresponding to those illustrated in Figures 1 and 2). The displacements are given relative to the cubic lattice parameter, $a = 5.43$ Å. A negative displacement indicates relaxation inward (i.e., toward the defect). We use T, H, H*, and S to refer to tetrahedral, hexagonal, bond-centered, and split forms, respectively. D and D' refer to the stable and metastable divacancies. We designate the Frenkel defects according to "vacancy type + interstitial type".

Table II: Activation energy data for migration of point defects. The energy differences were obtained from the numerical values calculated by the migration simulation program. We have given two energies and a sequence of sites describing the corresponding migration paths for the H*-interstitial and S-interstitial defects. Some of the defects are unstable with respect to migration, which suggests that these configurations are multidimensional saddle points rather than true energy minima.

Table I

Defect	Tersoff 2 ΔE_f (eV)	Tersoff 2 δ_i/a	Tersoff 3 ΔE_f (eV)	Tersoff 3 δ_i/a
vacancies				
T	2.81	0.0043	3.70	0.045
S	1.46	–0.080	3.52	–0.050
divacancies				
D	4.22	0.0043	5.57	0.044
D'	6.22	δ_1/a=0.0049	7.64	δ_1/a=0.045
		δ_2/a=0.0049		δ_2/a=0.031
interstitials				
T	5.04 (4.0)	δ_1/a=0.032	3.48	δ_1/a=(0)
		δ_2/a=(0)		δ_2/a=0.045
H	3.68	0.032	4.63	0.043
H*	3.50	δ_1/a=0.036	4.08	δ_1/a=0.040
		δ_2/a=0.021		δ_2/a=0.027
		δ_3/a=0.013		δ_3/a=0.019
S	2.46	δ_1/a=0.082	4.41	δ_1/a=0.063
		δ_2/a=0.074		δ_2/a=0.048
		δ_3/a=0.019		δ_3/a=0.027
Frenkel				
T+T	7.85		7.19	
T+H	6.49		8.34	
T+H*	6.31		7.78	

Table II

Point Defect Type	Tersoff 2 ΔE_m (eV)	Tersoff 3 ΔE_m (eV)
vacancies		
T	0.25	2.5
S	1.60	2.7
divacancies		
D	2.2	3.6
D'	0.21	1.55
interstitials		
T	unstable	1.1
H	unstable	unstable
H*	0.5 (H*→T→H*)	0.56 (H*→H→H*)
	0.17 (H*→H→H*)	0.02 (H*→T→H*)
S	1.5 (S→H*→T→H*→S)	0.27 (S→T→S)
	1.2 (S→H*→S)	

Figure Captions

Figure 1: This figure shows the four different vacancy configurations: (a) tetrahedral and (b) split monovacancy structures, and the (c) stable and (d) metastable divacancy structures, designated T, S, D, and D', respectively. The atoms around the tetrahedral vacancy relax outwards from their initial locations by a distance $\delta = 0.0043a$ ($a = 5.43$ Å is the cubic lattice parameter) for T2 and by $\delta = 0.045a$ for T3. In the split structure, one of the atoms next to the vacant tetrahedral site moves halfway towards the empty site, thus splitting the vacancy between two sites. The surrounding atoms relax inwards toward the site opposite the intermediate atom by $\delta = 0.080a$ for T2 and by $\delta = 0.050a$ for T3. The divacancy formation energies are largely consistent with the number of bonds broken, and the relaxation of the atoms surrounding the divacancy is similar to that observed for T-vacancies. The atoms around the D'-divacancy relax by different amounts, so the figure shows two displacements, δ_1 and δ_2.

Figure 2: Four interstitial structures are shown. Figure (a) shows the tetrahedral (T) structure, (b) shows the hexagonal (H) structure, (c) shows the alternate bond-centered or axial hexagonal (H*) structure, and (d) shows the split-site form. The interstitial atoms in (a)-(c) are white and marked with an "I", while in (d) the two atoms that form the split structure are white and marked with "S". The figures also show how sets of atoms around the defect relax. Each set consists of atoms that relax with the same size of displacement (shown as vectors with length δ_i). When we show more than one set, we have ranked them in decreasing order of displacement magnitude and marked the members of each set with a number corresponding to their rank. The H*- and S- interstitial structures have relaxation displacements that are significant for

more atoms than for the T- and H- interstitials, so we have indicated up to three different displacements. Note that for the T2 potential, only the nearest neighbors undergo any appreciable relaxation around a T-interstitial, while for the T3 potential, these atoms move very little and the atoms in the second neighbor shell move outwards.

Figure 3: Paths selected to simulate (a) vacancy and (b) divacancy migration.

Figure 4: The two graphs show the results of the vacancy migration calculations for bulk silicon. We present the vacancy energy both before and after relaxation as it migrates from one T-site to an adjacent one for (a) T2 and (b) T3. Note that the vacancy switches to the split form in mid step.

Figure 5: The two graphs show the energy as a divacancy migrates in bulk silicon via the process illustrated in Figure 3b. The energy before and after relaxation is shown for (a) T2 and (b) T3.

Figure 6: The graphs show the interstitial energy as the defect migrates from one tetrahedral site to an adjacent one in bulk silicon. Note that the H*- and H-sites lie along this path. The unrelaxed and relaxed energies are presented for (a) T2 and (b) T3.

Figure 7: The arrows illustrate the first half of the S-interstitial migration process: the atom labeled "1" moves into the vacant T-site (shown as a white circle), which causes the other atom comprising the split interstitial (labeled "2") to move to a nearby interstitial position (such as T or H*), converting the S-interstitial to one of the other types. The second half of the migration step is an analogous inverse process that converts the simple interstitial into a split interstitial about a nearby T-site.

Figure 8: The graphs show the vacancy migration energies as the defect migrates inwards from [111] and [100] type surfaces both before relaxation (ur) and after relaxation (r) of the surrounding atoms. Illustrated are migration from [111] for T2(a) and T3(b), and migration from [100] for T2(c) and T3(d). The steps indicated on the horizontal axes correspond to completed hops from tetrahedral site to tetrahedral site. Each site is successively deeper into material.

Figure 9: The graphs show the interstitial migration energies as the defect migrates inwards from [111] and [100] type surfaces both before relaxation (ur) and after relaxation (r) of the surrounding atoms. Illustrated are migration from [111] for T2 (a) and T3 (b); and migration from [100] for T2 (c) and T3 (d). The steps indicated on the horizontal axes correspond to completed hops from tetrahedral site to tetrahedral site. Each site is successively deeper into the material.

Figure 10: The graphs illustrate the formation of the T-vacancy/T-interstitial Frenkel defect for (a) T2 and (b) T3. We show both relaxed and unrelaxed curves.

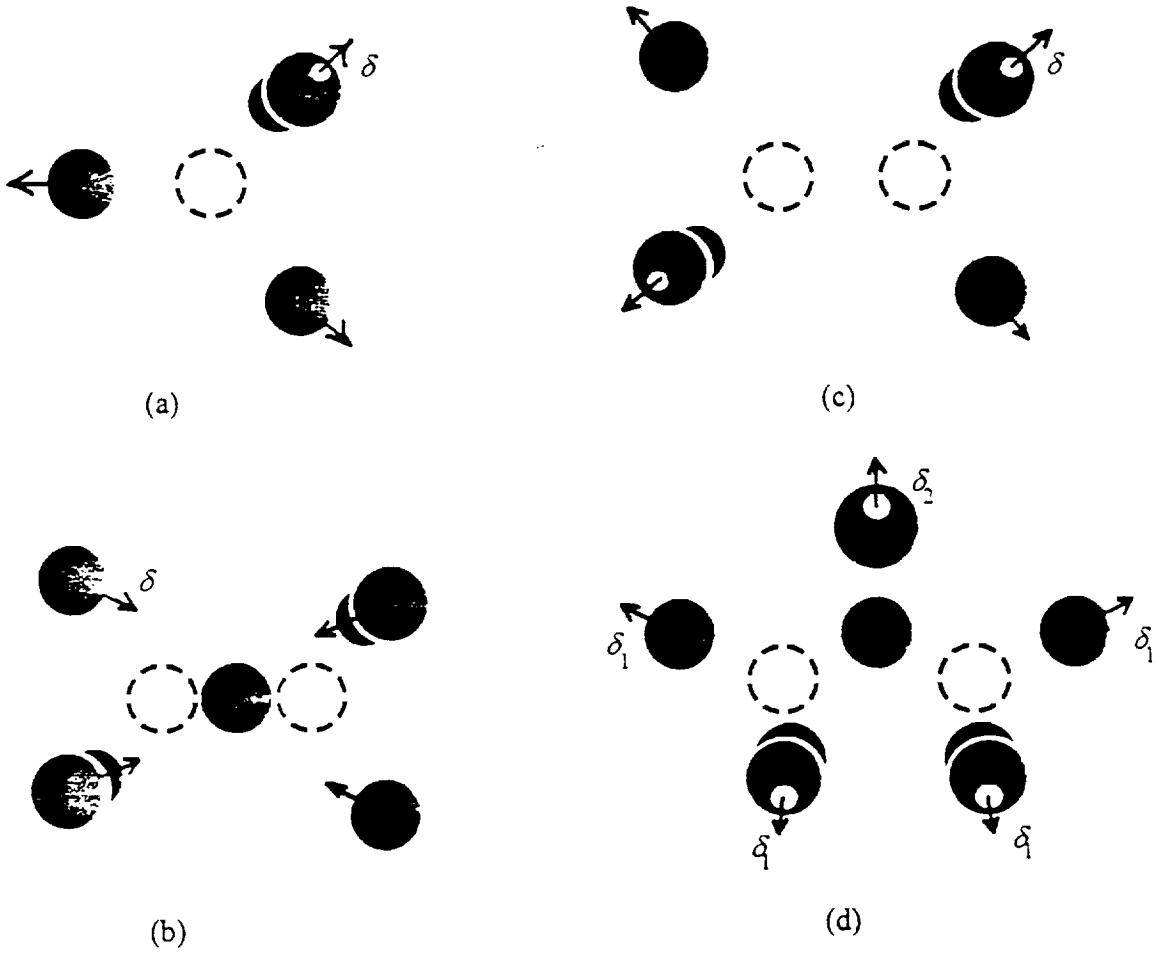

Figure 1

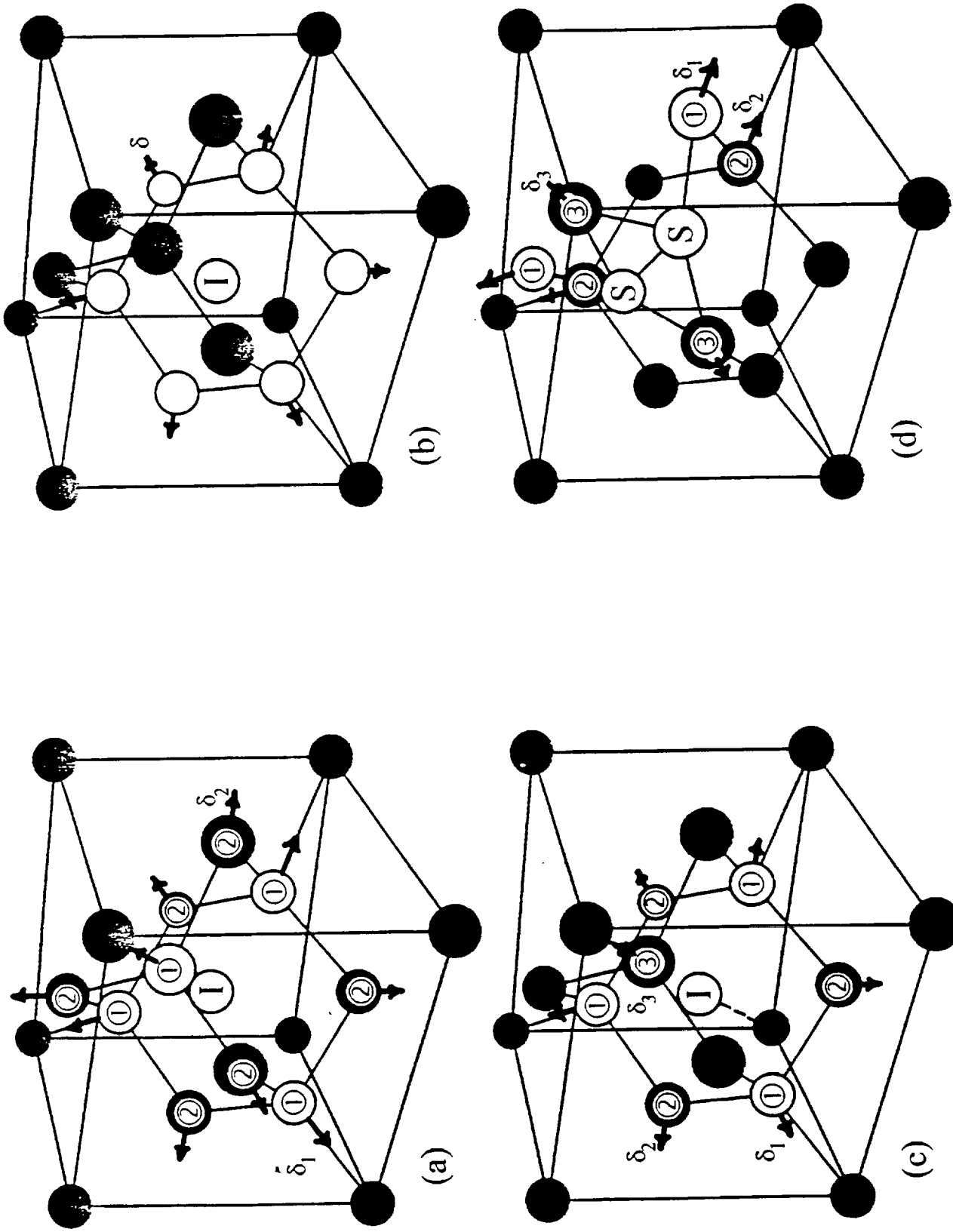

Figure 2

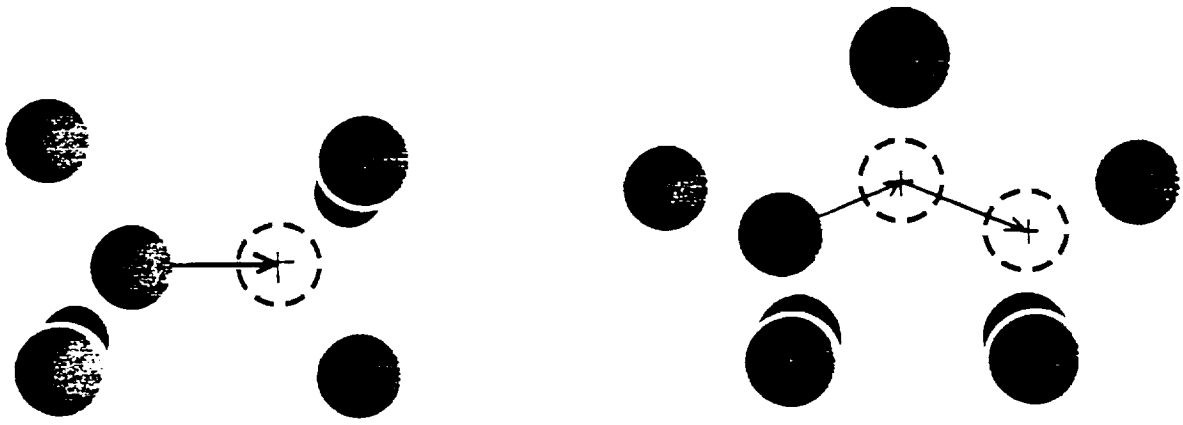

(a) (b)

Figure 3

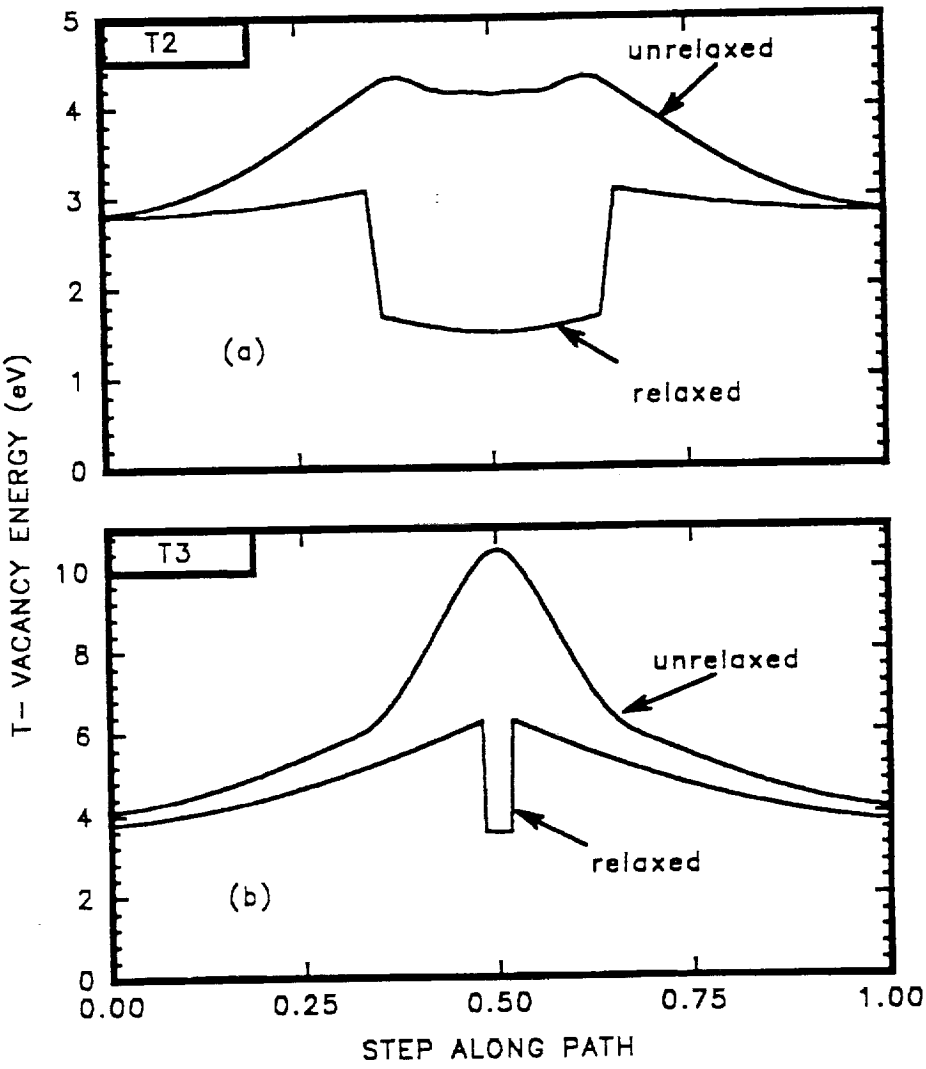
T2
unrelaxed
(a)
relaxed
T3
unrelaxed
relaxed
(b)
T- VACANCY ENERGY (eV)
STEP ALONG PATH
0
1
2
3
4
5
0
2
4
6
8
10
0.00
0.25
0.50
0.75
1.00

Figure 4

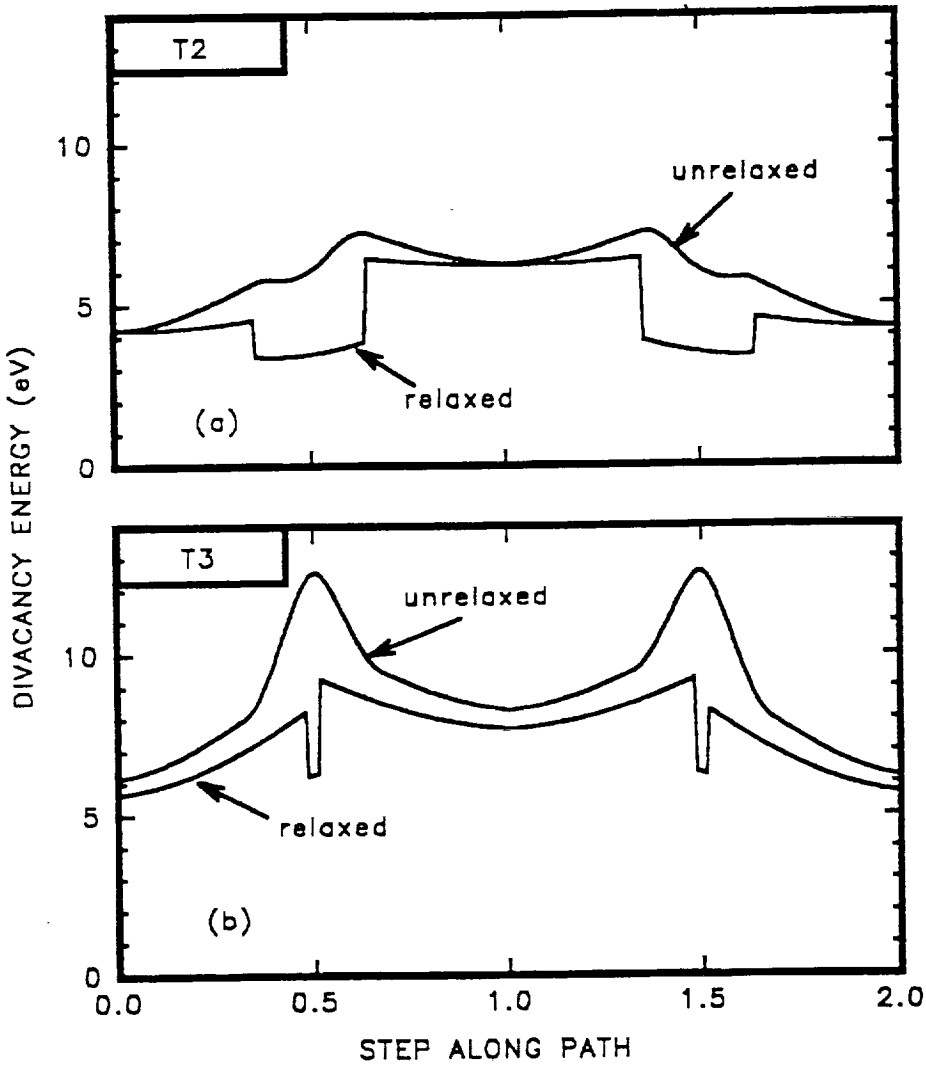
T2
10
5
0
unrelaxed
relaxed
(a)
T3
unrelaxed
10
5
relaxed
(b)
0
0.0
0.5
1.0
1.5
2.0
DIVACANCY ENERGY (eV)
STEP ALONG PATH

Figure 5

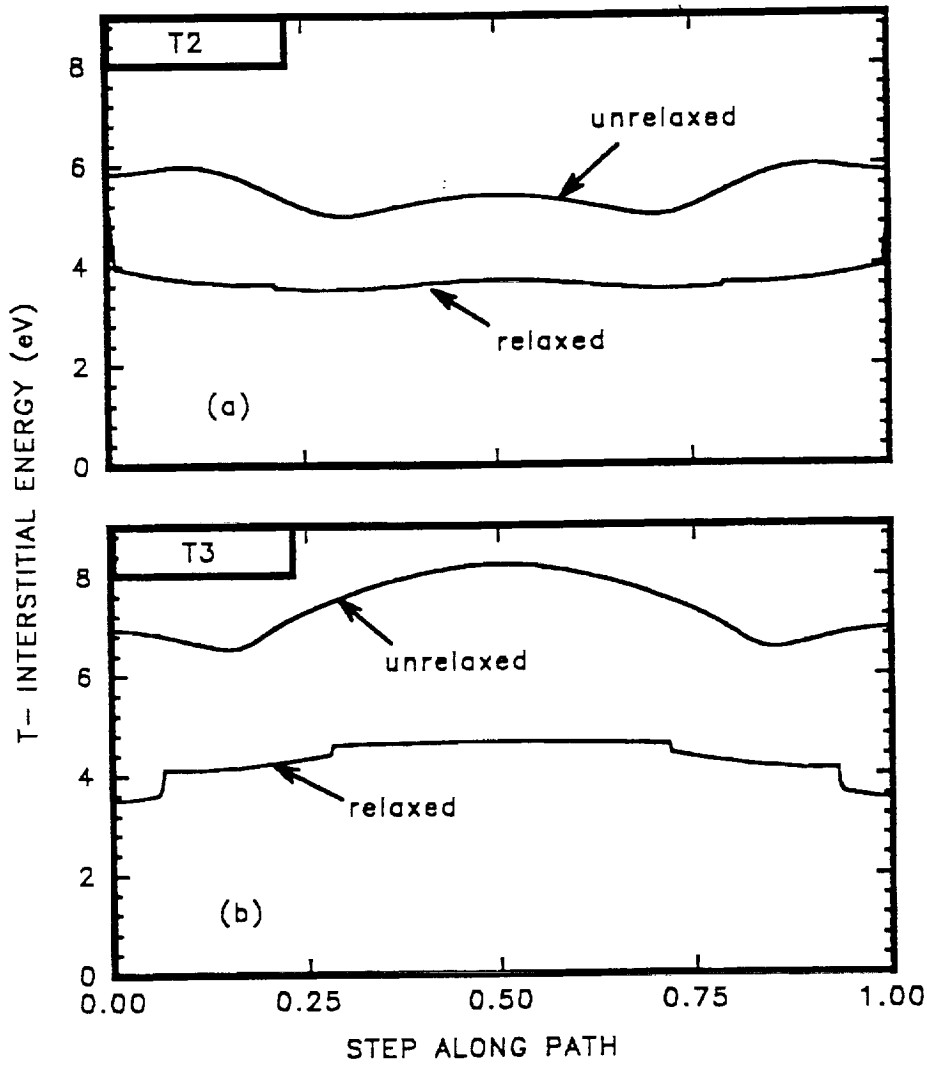
T2
unrelaxed
relaxed
(a)
T3
unrelaxed
relaxed
(b)
T- INTERSTITIAL ENERGY (eV)
0
2
4
6
8
0.00
0.25
0.50
0.75
1.00
STEP ALONG PATH

Figure 6

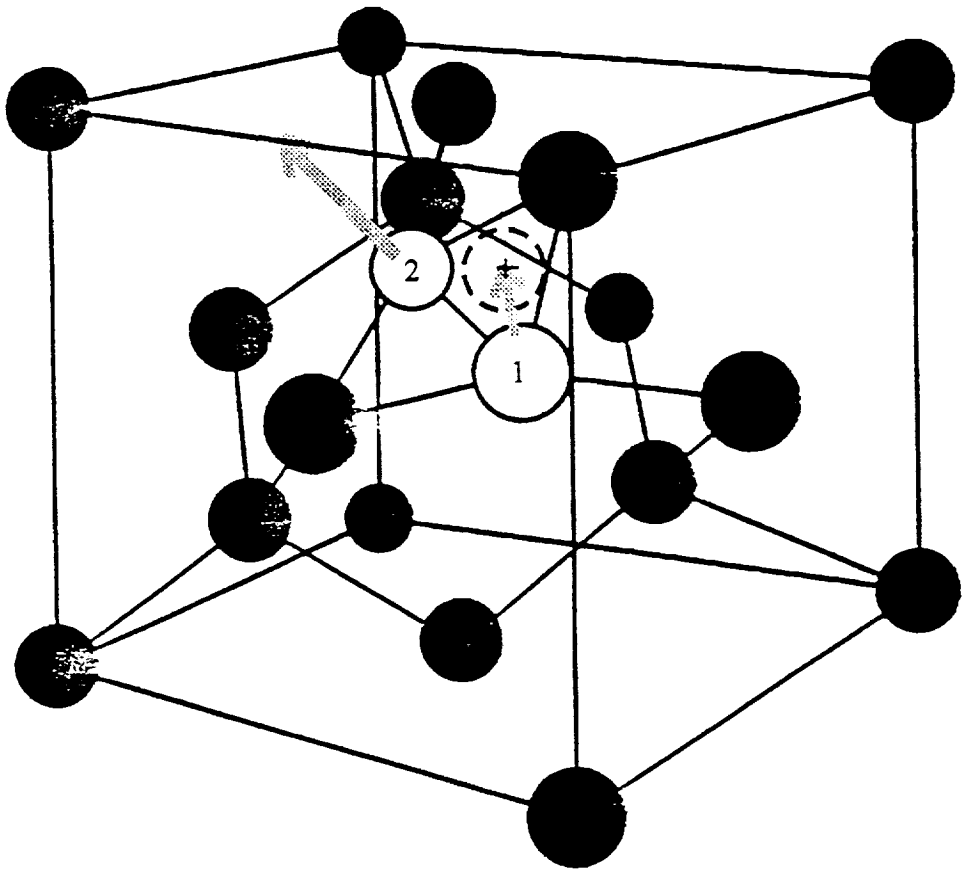

Figure 7

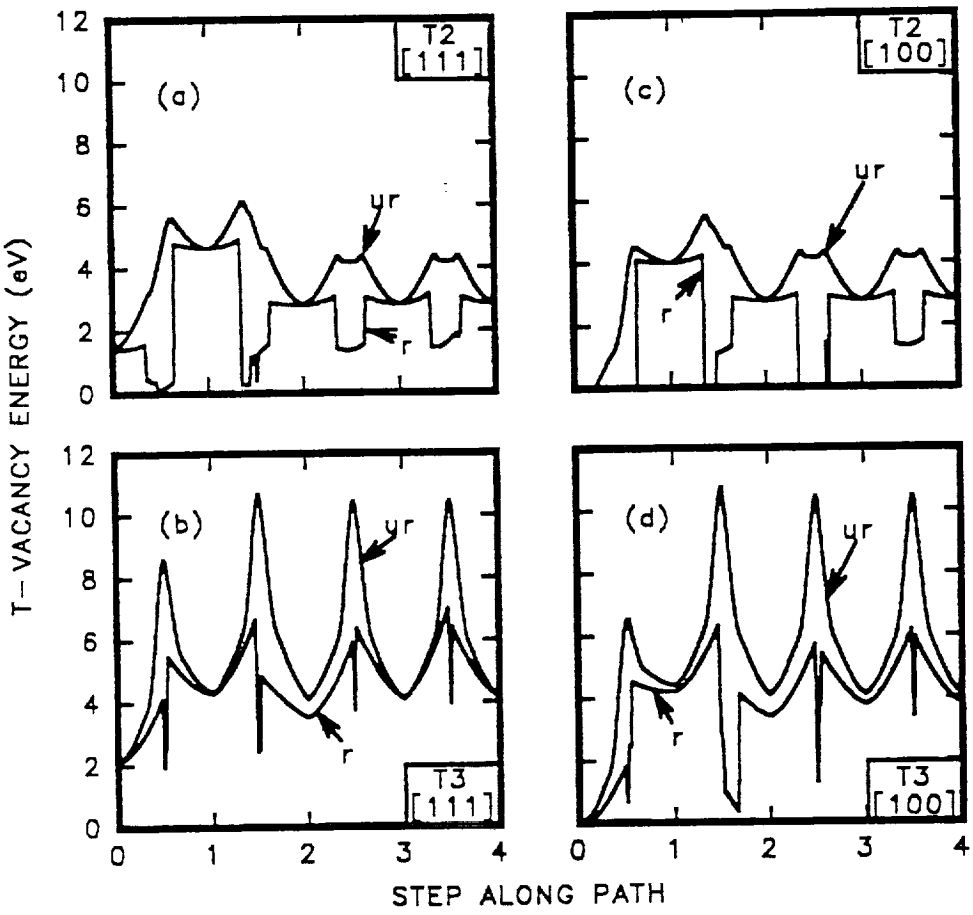
T2
[111]
(a)
ur
r
T2
[100]
(c)
ur
r
(b)
ur
r
T3
[111]
(d)
ur
r
T3
[100]
T- VACANCY ENERGY (eV)
STEP ALONG PATH
0
2
4
6
8
10
12
0
1
2
3
4

Figure 8

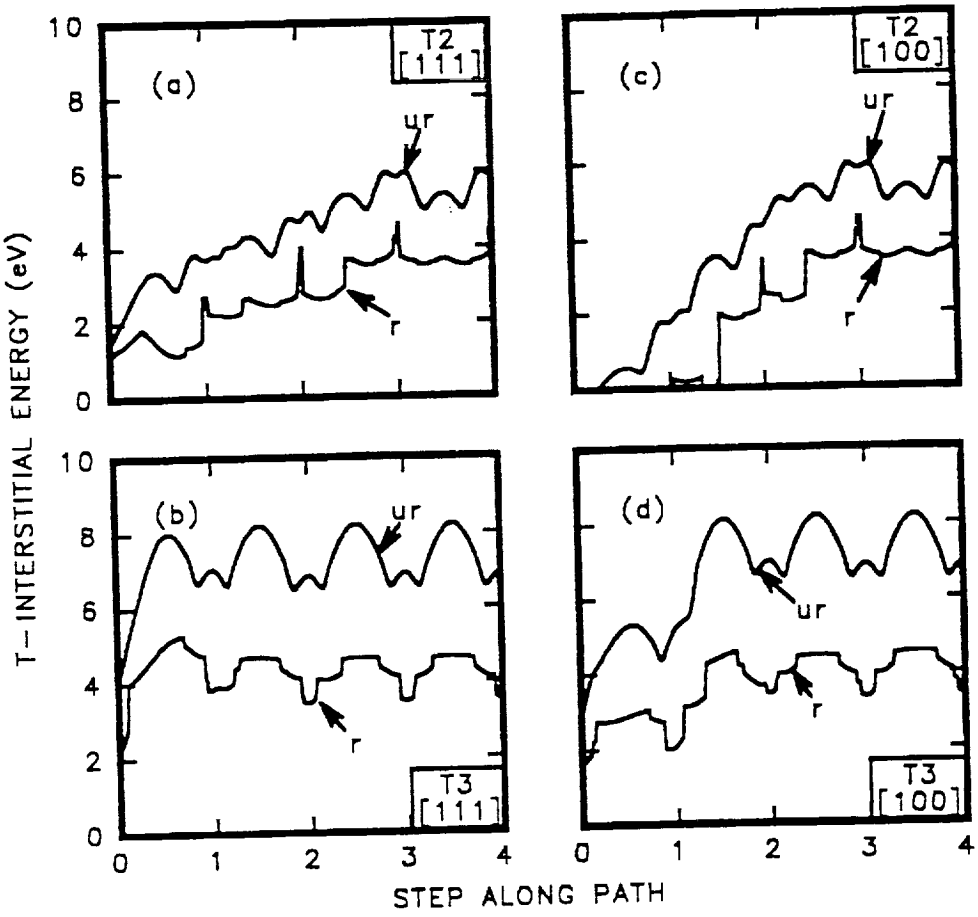
T2
[111]
(a)
ur
r
T2
[100]
(c)
ur
r
(b)
ur
r
T3
[111]
(d)
ur
r
T3
[100]
T-INTERSTITIAL ENERGY (eV)
STEP ALONG PATH
0
2
4
6
8
10
0
1
2
3
4

Figure 9

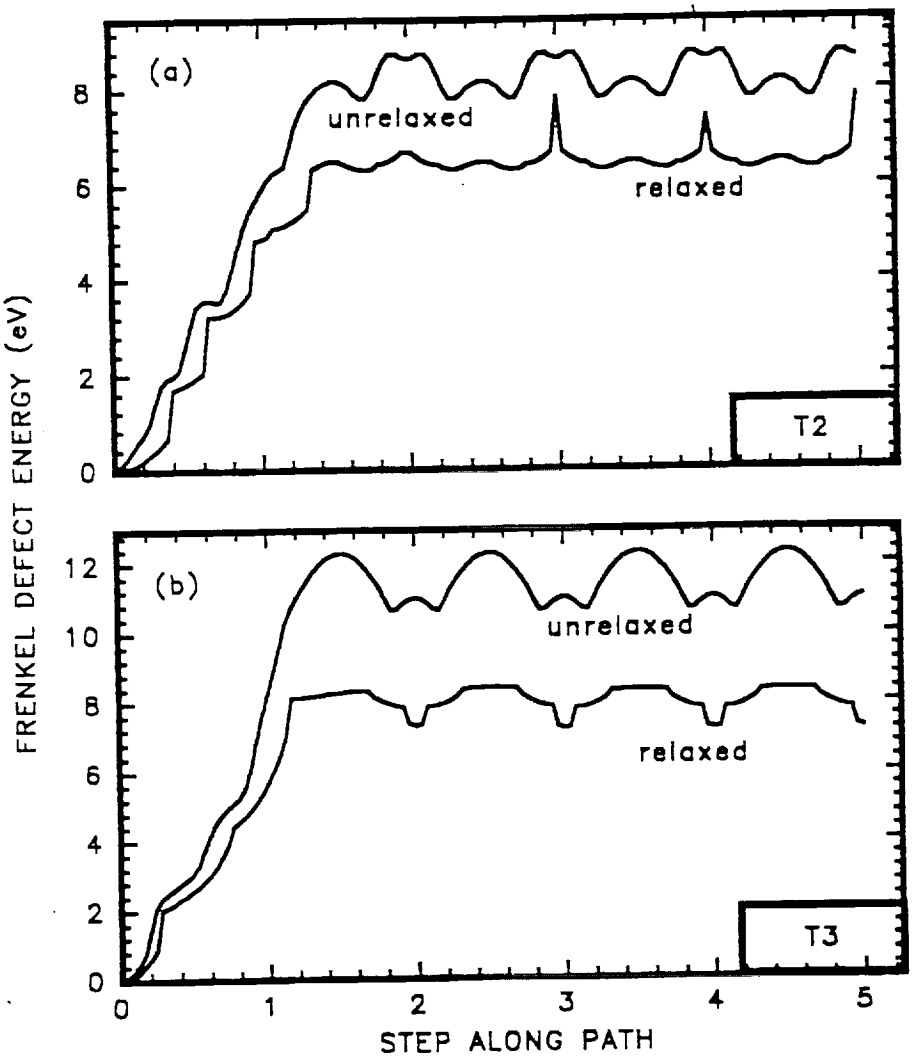
(a)
unrelaxed
relaxed
T2
(b)
unrelaxed
relaxed
T3
FRENKEL DEFECT ENERGY (eV)
STEP ALONG PATH
0
2
4
6
8
10
12
1
3
5

Figure 10